Recovering the second moment of the strain distribution from neutron Bragg edge data

K. Fogarty, E. Ametova, G. Burca, A.M. Korsunsky, S. Schmidt, P.J. Withers, and W.R.B Lionheart

Published version information

Citation: K Fogarty et al. Recovering the second moment of the strain distribution from neutron Bragg edge data. Appl Phys Lett 120, no. 16 (2022): 164102.

DOI: 10.1063/5.0085896

Applied Physics Letters

Recovering the second moment of the strain distribution from neutron Bragg edge data

Cite as: Appl. Phys. Lett. **120**, 164102 (2022); https://doi.org/10.1063/5.0085896
Submitted: 20 January 2022 • Accepted: 07 April 2022 • Published Online: 21 April 2022

K. Fogarty, E. Ametova, G. Burca, et al.

Applied Physics Letters ARTICLE scitation.org/journal/apl

Recovering the second moment of the strain distribution from neutron Bragg edge data

Cite as: Appl. Phys. Lett. **120**, 164102 (2022); doi: 10.1063/5.0085896
Submitted: 20 January 2022 · Accepted: 7 April 2022 ·
Published Online: 21 April 2022

K. Fogarty,[1,2] E. Ametova,[1,3] G. Burca,[1,4] A. M. Korsunsky,[5] S. Schmidt,[6] P. J. Withers,[7] and W. R. B. Lionheart[1,a)]

AFFILIATIONS

[1]Department of Mathematics, The University of Manchester, Manchester M13 9PL, United Kingdom
[2]Department of Physics and Astronomy, The University of Manchester, Manchester M13 9PL, United Kingdom
[3]Laboratory for Application of Synchrotron Radiation, Karlsruhe Institute of Technology, Karlsruhe 76131, Germany
[4]ISIS Pulsed Neutron and Muon Source, STFC, UKRI, Rutherford Appleton Laboratory, Didcot OX11 0QX, United Kingdom
[5]Department of Engineering Science, University of Oxford, Oxford OX1 3PJ, United Kingdom
[6]European Spallation Source, Lund S-221 00, Sweden
[7]Henry Royce Institute, Department of Materials, The University of Manchester, Manchester M13 9PL, United Kingdom

[a)]**Author to whom correspondence should be addressed:** bill.lionheart@manchester.ac.uk

ABSTRACT

Point by point strain scanning is often used to map the residual stress (strain) in engineering materials and components. However, the gauge volume and, hence, spatial resolution are limited by the beam defining apertures and can be anisotropic for very low and high diffraction (scattering) angles. Alternatively, wavelength resolved neutron transmission imaging has a potential to retrieve information tomographically about residual strain induced within materials through measurement in transmission of Bragg edges—crystallographic fingerprints whose locations and shapes depend on microstructure and strain distribution. In such a case, the spatial resolution is determined by the geometrical blurring of the measurement setup and the detector point spread function. Mathematically, reconstruction of the strain tensor field is described by the longitudinal ray transform; this transform has a non-trivial null-space, making direct inversion impossible. A combination of the longitudinal ray transform with physical constraints was used to reconstruct strain tensor fields in convex objects. To relax physical constraints and generalize reconstruction, a recently introduced concept of histogram tomography can be employed. Histogram tomography relies on our ability to resolve the distribution of strain in the beam direction, as we discuss in the paper. More specifically, Bragg edge strain tomography requires extraction of the second moment (variance about zero) of the strain distribution, which has not yet been demonstrated in practice. In this paper, we verify experimentally that the second moment can be reliably measured for a previously well characterized aluminum ring and plug sample. We compare experimental measurements against numerical calculation and further support our conclusions by rigorous uncertainty quantification of the estimated mean and variance of the strain distribution.

Residual stress (and thereby elastic strain) is the stress that remains in a body when no external forces are applied.[1] Because these internal stresses add to those arising from externally applied loads, if they are not detected they can give rise to unexpected behaviors and premature failure. Therefore, information about the strain measured within polycrystalline materials is critically important for understanding the deformation and fracture mechanics of engineered components. A well-established technique used for strain measurements is based on neutron diffraction (or Bragg scattering). Depending on the material, the scattered neutrons will constructively interfere with each other only in particular directions and produce an intensity pattern (the so-called Bragg peaks) from which the structure of the material is derived. Measurement of the position of Bragg peaks from diffraction allows the determination of lattice spacings, while the measurement of the relative shift in the positions provides information on lattice strains.[2] To achieve high spatial resolution, a sample is raster scanned with a collimated or focused beam and the angle of scattered beam 2θ (e.g., angle-dispersive diffraction) or wavelength/energy (e.g., energy-dispersive diffraction) is recorded to deduce the interplanar spacing, point by point, using Bragg's equation. This is then used to infer strain

based on a comparison with the reference interplanar spacing. To overcome some of the disadvantages given by neutron diffraction measurements (e.g., slow acquisition, the uncertainty of the exact specimen or gauge location along the beam[3]), a new technique called Bragg edge neutron transmission for strain measurements was proposed and demonstrated.[4,5]

In this respect, a polychromatic neutron beam in a combination with a Time-of-Flight (ToF) area detector can be employed to register both spatial and ToF (wavelength) information about the transmitted neutrons. According to Bragg's law,

$$2d_{hkl}\sin\theta = \lambda_{hkl}, \tag{1}$$

coherent elastic scattering at an incident angle of θ can happen only for wavelengths λ shorter than twice the spacing between the lattice planes (d_{hkl}). Hence, the transmitted spectrum will exhibit a rapid increase in the transmitted intensity at a wavelength λ slightly longer than twice this distance because intensity can no longer be diffracted out of the transmitted beam by this *hkl* family of planes. This sharp change in transmission is called a Bragg edge and allows the establishment of a relationship between the transmitted neutron spectral fingerprint and the crystallographic phases in the material. The application of the Bragg edge neutron transmission for strain mapping has been recently extended to high spatial resolutions due to advances in micro-channel-plate (MCP) detector technology.[6,7]

Given a sample rotation, a strain tensor field in the object can be reconstructed tomographically (in general, rotations about six directions that do not lie on a projective conic are required to reconstruct tensor field[8]). This technique is referred to as Bragg edge strain tomography and seeks to determine the spatial distribution of strain inside a polycrystalline sample from the change in the neutron transmission spectra near a Bragg edge.[3,8–11] Given ideal conditions and a uniformly strained material, the Bragg edge can be modeled as a Heaviside function multiplied by a linear function of wavelength.[12] The result of this uniform strain is to shift the relative position (mean) of the Bragg edge with respect to that for a sample without strain present. However, the mean cannot provide sufficient information to resolve the strain distribution along the ray path,[8] i.e., there are infinitely many distributions of the strain fields along the beam path, which will produce the same mean. This problem is related to a non-trivial null-space of the longitudinal ray transform, which gives a mathematical foundation for Bragg edge strain tomography,[8] i.e., the mean measurements do not uniquely determine strain tensor fields. To overcome this problem, tomographic data can be combined with equilibrium equations of elasticity using a finite element approach to find the strain.[11] Alternatively, Lionheart[12] observed that an experimentally measured Bragg edge is representative of the cumulative strain histogram along a neutron ray within the material. Hence, differentiation of the Bragg edge will theoretically return the histogram of strain, i.e., the distribution of strain components collinear with the ray discretized into bins. The shape of the histogram is the convolution of the histogram for the unstrained case with the histogram of the relevant component of strain along the beam, and the second moment of the deconvolved histogram is the ray transform of the symmetric second tensor power of the strain. Hence, the histogram longitudinal ray transform[12] can be used to reconstruct the strain tensor in every voxel. The proposed theoretical method relies on our ability to measure the second moment of the strain distribution in transmission (projection) data, which has not yet been demonstrated in practice.

In this paper, we demonstrate that the second moment, the variance about zero, of strain in the ray direction can be captured experimentally. We present an analysis of two reference samples [Fig. 1(a)] manufactured within the Versailles Project on Advanced Materials and Standards (VAMAS).[13] The first sample is a shrink-fit aluminum alloy assembly of ring and plug (henceforth the strained sample). The ring and the plug have outer diameters of 50 and 25 mm, respectively. The second sample is an unstained plug of the same diameter (henceforth the strain-free sample). Both samples were manufactured under well controlled conditions and are of weak crystallographic texture and low residual stress prior to assembly. In addition, they have been extremely well characterized in a global round-robin study.[14]

In order to compare experimental measurements with theoretical predictions, we briefly recall some details about the expected strain in the strained sample. The axial stress of the plug, σ^p_{zz}, the ring σ^r_{zz}, and the interface pressure, P, has been determined in a series of neutron diffraction strain experiments[14] and has been found to be -15, 5, and 48 MPa, respectively. The values of Poisson's ratio, ν, and the Young's

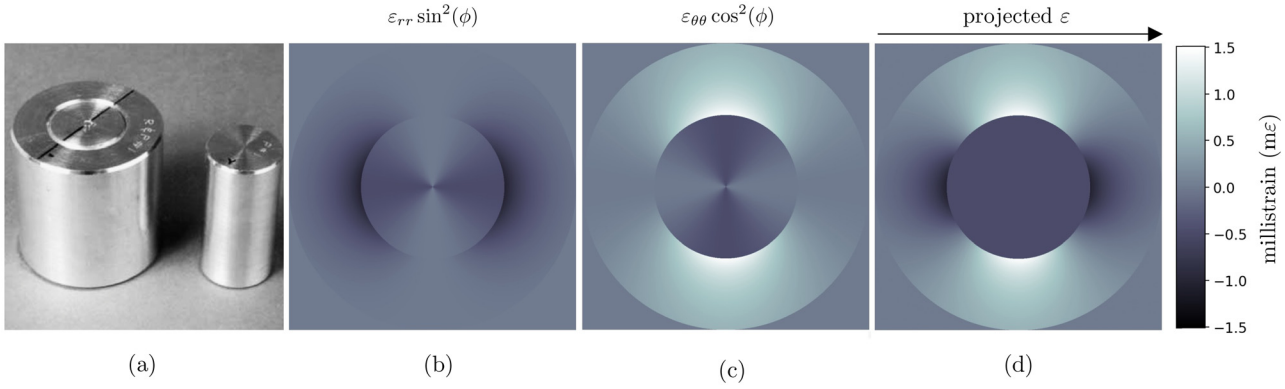

FIG. 1. (a) VAMAS round robin shrink fitted aluminum ring-and-plug and plug test samples (figure taken from the VAMAS report[16]) and (b) ε_{rr} component of the strain tensor scaled by $\sin^2\phi$. (c) $\varepsilon_{\theta\theta}$ component of the strain tensor scaled by $\cos^2\phi$. (d) Plot of the expected strain ($\varepsilon = \varepsilon_{\theta\theta}\cos^2\phi + \varepsilon_{rr}\sin^2\phi$) within the strained sample for a ray path indicated by the arrow above the figure.

modulus, E, of the material were taken to be 0.33 and 68 GPa, respectively. The radial and hoop strain can be obtained via solving the governing equations of linear elastic theory.[15] Assuming that the axis of the cylinder is perpendicular to the direction of travel of the sufficiently parallel neutron beam, the strain along the ray path, ε, is related to the radial (ε_{rr}) and hoop ($\varepsilon_{\theta\theta}$) components of strain via $\varepsilon = \varepsilon_{rr} \sin^2 \phi + \varepsilon_{\theta\theta} \cos^2 \phi$, where ϕ is the angle anticlockwise from the neutron direction of travel. We will refer to the resulting distribution of strain as the projected strain. We discretize the analytical strain map onto the experimental detector grid and sample from this array to calculate the first and the second moments of the distribution along the ray path. Figures 1(b)–1(d) show the individual contour maps of the two calculated components of strain and their sum.

The sample was measured[17] at the Imaging and Materials Science & Engineering (IMAT) beamline operating at the ISIS spallation neutron source (Rutherford Appleton Laboratory, UK).[18,19] At a pulsed neutron source, the wavelengths of the detected neutrons are calculated from their time of flight by

$$\lambda = \frac{h(T + \Delta T_0)}{mL}, \tag{2}$$

where λ is the neutron wavelength (in meters), h is Planck's constant, T is the neutron time of flight (in seconds), ΔT_0 is the time offset of the source trigger received by the data processing electronics (in seconds), m is the neutron mass (in kilograms), and L is the flight path from source to the detector (in meters). The MCP detector[6,20] used for the experiment was configured to record 2897 wavelength channels between 3.12 and 5.12 Å giving access to lattice planes from 1.56 to 2.56 Å in d-spacing, which for aluminum are the 111 and 200 lattice planes. To reduce the undesirable effect of counts loss,[21] two shutter intervals were set in the ToF (wavelength) domain with a resolution of 7.21×10^{-4} and 3.60×10^{-4} Å, respectively. The MCP detector has 512×512 pixels, 0.055 mm pixel size, giving a field of view of approximately 28×28 mm^2. A visible laser beam was used to align the cylinder axis of the sample with respect to the vertical edge of the detector and to ensure that the plug, the ring and their interface are in the field-of-view [Fig. 2(a)]. Subsequently, the strain-free reference sample was aligned and centered vertically and measured.

Individual projections of samples and a single normalization image were measured using 4 h long exposures. Flat-field and MCP detector related corrections[21] were adapted from BEAn[22] and applied to the projections. As the strained sample is axially symmetric, of weak crystallographic texture and only a radial-hoop internal stress exists, we assume that the strain does not vary along the cylinder axis. Consequently, we sum over each vertical column of pixels to improve the signal-to-noise ratio. Such aggregated pixels are commonly referred to as macro-pixels.

Given the measured wavelength range, two distinct Bragg edges were present in the acquired spectra, $\lambda \approx 4.0$ Å (200 lattice planes), and $\lambda \approx 4.7$ Å (111 lattice planes), with the latter one more pronounced and also sampled with higher wavelength resolution [Fig. 2(b)]. Therefore, we performed analysis only for the latter edge. To model the transmission spectra around the Bragg edge, we used the Santisteban function[23]

$$\mathrm{Tr}(\Lambda, \psi) = \exp\left(-(a_0 + b_0\Lambda)\right)\left(1 - \exp\left(-(a_1 + b_1\Lambda)\right)\right)B(\Lambda), \tag{3}$$

where Λ is the experimentally acquired transmission signal measured in Å and $\psi = (a_0, b_0, a_1, b_1)$ is a vector of the model parameters.

Here, a_0, b_0, and a_1, b_1 describe the exponential attenuation to the right (tail) and to the left (pedestal) of the Bragg-edge, respectively, and $B(\Lambda)$ is given by

$$B(\Lambda) = \frac{1}{2}\left[\mathrm{erfc}\left(-\frac{\Lambda - \lambda_{hkl}}{\sqrt{2}\sigma}\right) - \exp\left(-\frac{\Lambda - \lambda_{hkl}}{\tau} + \frac{\sigma^2}{2\tau^2}\right) \times \mathrm{erfc}\left(-\frac{\Lambda - \lambda_{hkl}}{\sqrt{2}\sigma} + \frac{\sigma}{\tau}\right)\right],$$

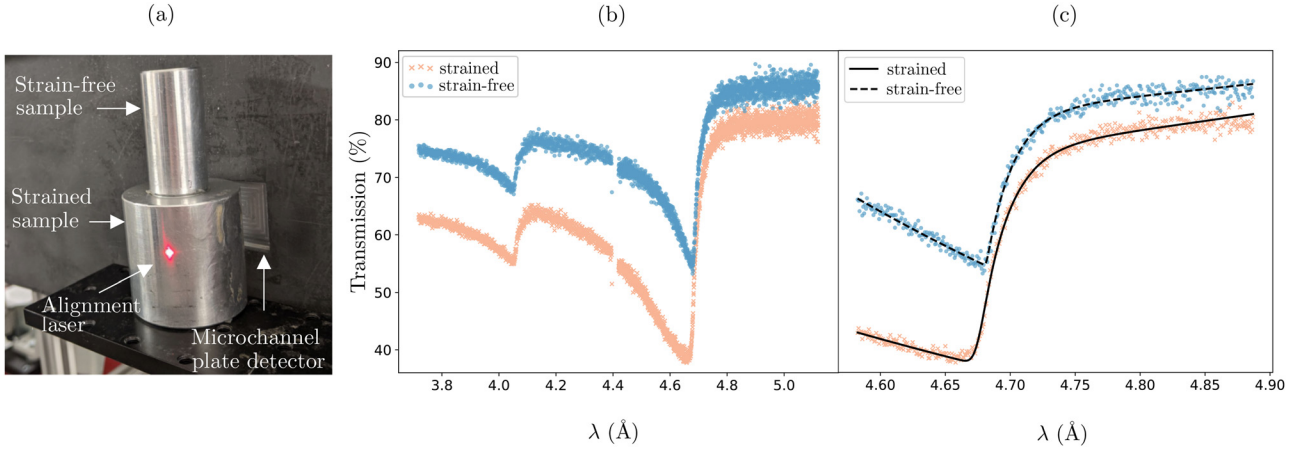

FIG. 2. (a) Scheme illustrating experimental data acquisition. (b) Plot showing the transmission of neutrons (%) in a single macro-pixel as a function of wavelength for both samples. Both curves are plotted with the same vertical axis. As samples have different diameters and have been positioned slightly differently (translationally), a pixel with the same index in both transmission images will correspond to a different penetration length through the material, hence, intensity. Therefore, there is a vertical offset between the two plotted curves. A gap in the recorded spectra is caused by detector readout between two shutter intervals. (c) Measured Bragg edge in a single macro-pixel overlaid with the fitted model function.

where λ_{hkl} is the position of the Bragg-edge, τ is the moderator decay constant, and σ is the Gaussian broadening due to the sample and instrument. See the supplementary material for derivation of the model.

The model[23] was not explicitly derived to account for strain but rather to model blur in the wavelength dimension due to the stochastic nature of neutron moderation and the geometric effects of the beamline.[24,25] Nevertheless, the sensitivity of the model to strain has been demonstrated in several studies.[26–29]

We used the non-linear least squares fitting (Levenberg–Marquardt algorithm) to fit the model function [Eq. (3)] and estimate parameters. To avoid the local minimum problem common to the non-linear fitting, we employ a three stage fitting process.[23] An example of a measured Bragg edge overlaid with the fitted model function is shown in Fig. 2(c).

The first moment (mean) of the projected strain is given by[30]

$$\langle \varepsilon \rangle = \frac{\lambda^s_{hkl} - \lambda^0_{hkl}}{\lambda^0_{hkl}}, \tag{4}$$

where λ^0_{hkl} and λ^s_{hkl} are the position of Bragg edge for the strain-free sample and the strained sample, respectively.

Our strategy for the measurement of the second moment (variance about zero) is as follows. The value of the moderator decay constant, τ, is a function of the geometry and temperature of the moderator used in the experiment;[22] as these parameters remained approximately constant within the experiment, τ is expected to be constant. Parameter σ is a function of width of the initial pulse from the moderator and sample-related broadening.[31] As the shape of the pulse is expected to be repeatable and uniform in the spatial dimension, any spatial change in σ can be attributed to the change in variance of strain in the beam direction. Although σ in Eq. (3) captures broadening of the Bragg edge, we need to establish a relationship between an instrument response and the variance of strain along a beam direction. Assuming a linear relationship, the model of measurements is given by $\mathrm{y} = m\mathrm{x} + c$, where $\mathrm{x} = [x_0, x_1, \ldots, x_{j-1}]$ is a vector of the theoretically predicted variance of strain in the beam direction at detector macro-pixel j between 0 and 511 and $\mathrm{y} = [\sigma_0, \sigma_1, \ldots, \sigma_{j-1}]$ is experimentally measured σ at each macro-pixel j. We use linear regression to define parameters m and c. Obviously, this simple proof-of-concept measurement model cannot substitute a proper instrument scale calibration necessary to establish this tomographic measurement technique.

To support our findings, we perform uncertainty quantification based on Bayesian interference.[32] In the Bayesian framework, the measurement model is represented as a joint probability distribution of unknown parameters $\boldsymbol{\eta}$ and observations $\mathbf{Y}$,

$$\pi(\boldsymbol{\eta}|\mathbf{Y}) = \frac{\pi(\mathbf{Y}|\boldsymbol{\eta})\pi(\boldsymbol{\eta})}{\pi(\mathbf{Y})}, \tag{5}$$

where $\pi(\mathbf{Y}|\boldsymbol{\eta})$ is the likelihood function of $\boldsymbol{\eta}$, i.e., the predictive distribution of $\mathbf{Y}$, given $\boldsymbol{\eta}$. The *prior* distribution $\pi(\boldsymbol{\eta})$ encodes the prior knowledge and model assumptions. The model evidence $\pi(\mathbf{Y})$ maps the likelihood, prior and observations to a single value that describes the probability of observation. Finally, $\pi(\boldsymbol{\eta}|\mathbf{Y})$ is the *posterior* probability: the probability of $\boldsymbol{\eta}$ after $\mathbf{Y}$ is observed.

The mean of the likelihood is given by the parametric model for each data point. Let j between 0 and 511 denote the position of a

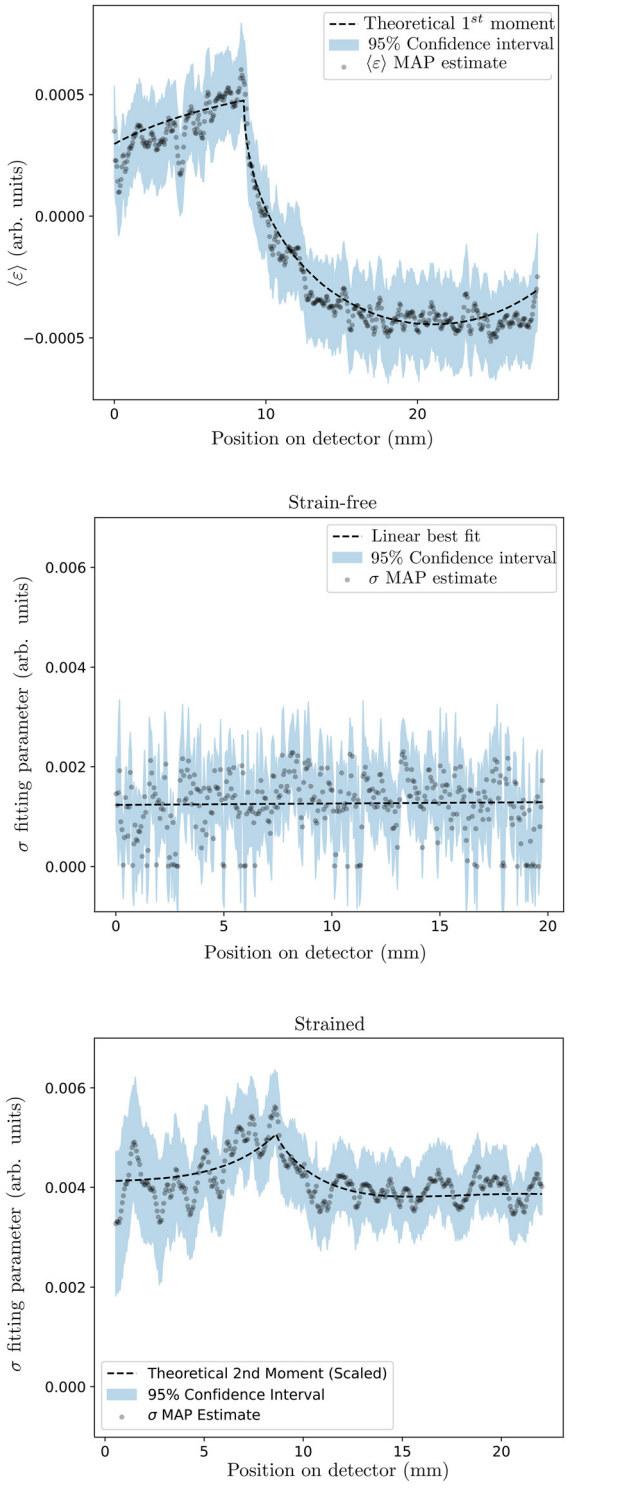

FIG. 3. Variation in the second moments as a function of detector pixel obtained via HMC Bayesian inference. MAP estimate refers to the position of the maximum posterior density, and the 95% is found from ±2 standard deviations of the posterior distribution.

column of pixels and $[\mathbf{Y}_j]_i = \mathrm{Y}(\lambda_i)_j$ be the mean measured transmission for wavelength bin i in pixel column j. We model the transmission error over a macro-pixel as additive Gaussian noise with zero mean and a variance that is linearly dependent on the transmission.[30] Then,

$$\mathrm{Y}(\lambda_i)_j = \mathrm{Tr}(\lambda_i|\boldsymbol{\psi}_j) + \xi(\omega|\lambda_i, j), \tag{6}$$

where $\xi(\omega|\lambda_i, j)$ is a Gaussian random variable

$$\xi(\omega|\lambda_i, j) \sim \mathcal{N}(0, s(\lambda_i)_j^2), \tag{7}$$

and $s(\lambda_i)_j^2$ is the unbiased estimate of the sample variance. Then, the likelihood $\pi(\mathbf{Y}|\boldsymbol{\eta})$ is given by

$$\pi(\mathrm{Y}(\lambda_i)_j|\boldsymbol{\psi}_j) = \pi(\xi(\omega|\lambda_i, j) = \mathrm{Y}(\lambda_i)_j - \mathrm{Tr}(\lambda_i|\boldsymbol{\psi}_j)) \tag{8}$$

$$\propto \exp\left(-\frac{1}{2}||\mathrm{Y}(\lambda_i)_j - \mathrm{Tr}(\lambda_i|\boldsymbol{\psi}_j)||_\Sigma^2\right), \tag{9}$$

where $||\cdot||_\Sigma^2$ is the covariance-weighted norm. Finally, we converge to

$$\pi(\mathrm{Y}(\lambda_i)_j|\boldsymbol{\psi}_j) = \exp\left(-\sum_{\lambda_i}\frac{1}{2s(\lambda_i)}\left(\mathrm{Y}(\lambda_i) - \mathrm{Tr}(\lambda_i|\boldsymbol{\psi}_j)\right)^2\right). \tag{10}$$

The prior distributions on the parameters of the model ψ_j are assumed to be weakly informative (wide peak) Gaussian's centered at the best estimates obtained from the Levenberg-Marquardt fit for each parameter. We further use the Hamiltonian Monte Carlo (HMC)[33] method to sample from the posterior distribution. Bayesian interference and HMC are implemented using the Python wrapper PySTAN for the probabilistic programming framework STAN.

Figure 3 compares a maximum *a posteriori* probability (MAP) estimation of the mean and second moment obtained from the experimental data. Overlaid we plot a confidence interval of two standard deviations of the distribution. For the strain-free case, parameter σ is expected to be constant but greater than 0 as σ also models blur in the wavelength dimension. Therefore, the theoretical predictions are given by the best linear fit to estimated data. Theoretical predictions for the strained sample are given by our calculations in Fig. 1, which were scaled linearly to best match data. It can clearly be seen that both mean and variance are within the uncertainty interval for both samples and the main trends are captured. However, there is strong noise present in all estimated parameters and for some data points the MAP estimate of the second moment is 0 and the 95% confidence interval includes negative values. There are several reasons for the observed behaviors.

Following Hendriks *et al.*,[30] we assumed Gaussian noise in the measured transmission data. In Fig. 4, we show the distribution of error in some representative macro-pixels overlaid with the fitted Gaussian probability density function. While the distributions have a clear bell-shape, they are also skewed toward negative values. Conducting a combined D'Agostino and Pearson's omnibus test[34] with a significance level of $\alpha = 0.001$ showed that of the 741 376 distributions considered 690 688 have enough evidence to reject the hypothesis that the data were drawn from a Gaussian distribution. The reason for this skew might be the overlap correction[21] used to compensate for counts loss. The correction relies on Poisson statistics, and the weighting factor for each wavelength bin is calculated based on values in shorter wavelength bins introducing inter-bin correlations and potentially a skew in the data.

The Santisteban model[23] was not designed to account for strain, and the parameter σ, which was used in this study as a measure of strain variance, does not have any physical meaning in the model. Second, the model assumes the Gaussian distribution of strain. In Fig. 5, we show a posterior distribution of σ for both samples. For the strained sample, we chose a data point where the fitting resulted in $\sigma = 0$. The posterior distribution is concentrated at $\sigma = 0$, consistent with the least-square fit. For the strain-free sample, the posterior distribution is multimodal with two pronounced peaks. Both distributions highlight inadequacy of the Santisteban model for uniquely identifying the second moment of the strain distribution. Therefore, more research is needed to have more accurate physical Bragg edge models for strain measurements.

While the demonstration in this paper is limited to a texture-free sample, the strain reconstruction approach[12] is applicable to a more general case of a textured sample. In the general case, we need to decouple various crystallographic information encoded in the measured Bragg edges. The actual shape of a Bragg edge in transmitted neutron beam reflects the crystal structure averaged along the beam path. With the current Bragg edge model, we explicitly assume that the strain distribution along the beam path is Gaussian. Second,

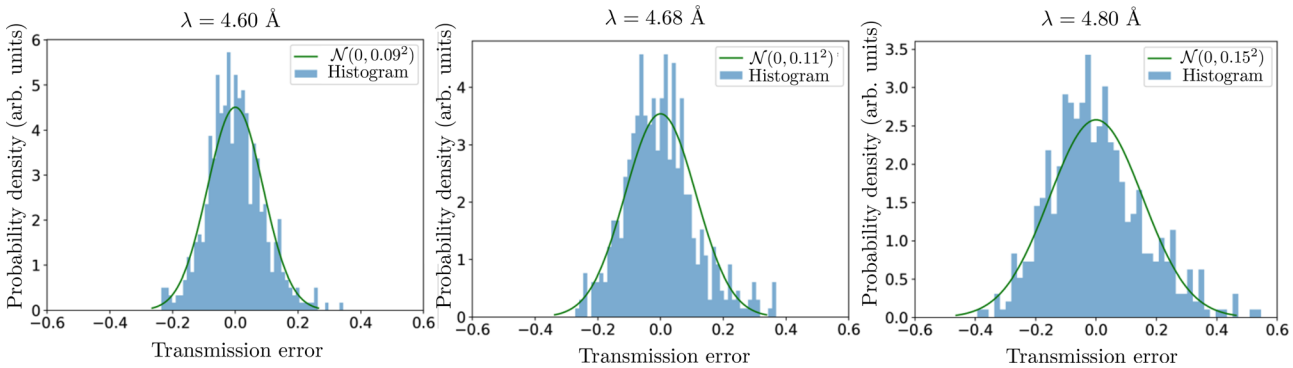

FIG. 4. Histograms showing the distribution of the error for different values of transmission for the central column of the detector pixels. A Gaussian probability density function has been fitted to the data (solid line).

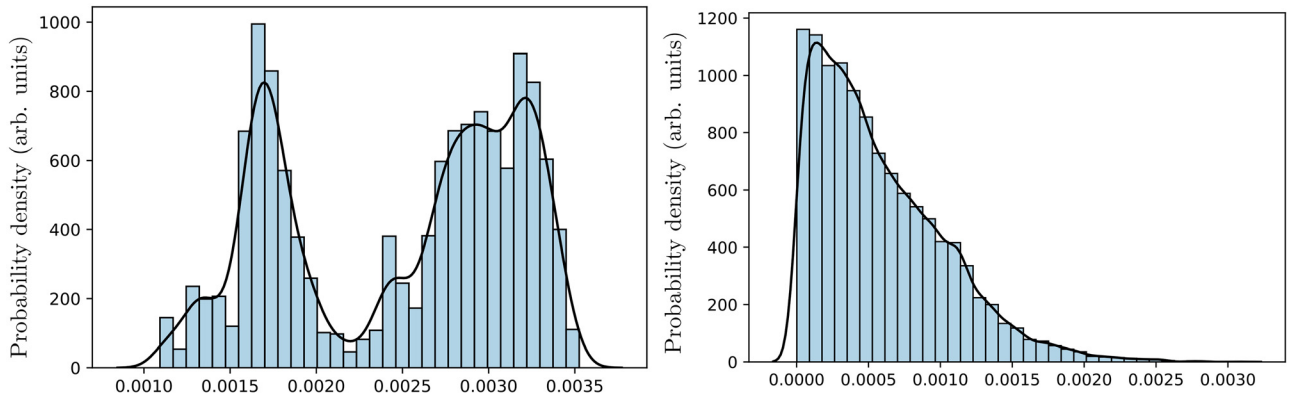

FIG. 5. Histograms of the posterior density of the σ parameter for detector column 110 of the strain-free sample (left) and for detector column 90 of the strained sample (right) shown; the solid line shows the kernel density estimate plot for the same distribution.

crystallographic texture (significant preferred orientation of crystallites) might not be properly handled by the current Bragg edge model. The texture affects the number of crystallites for which the backscattering condition is fulfilled.[4,35] Hence, it will affect the edge's pedestal, tail, and height. The current Bragg edge model was not designed to account for these effects and might not fit the data in the presence of significant texture. Hence, either a more accurate physical modeling of a Bragg edge is needed to decouple the effects of texture and strain on the Bragg edge, or direct derivation and deconvolution of Bragg edge data can be used. With the current measurement setup, the later method is not feasible due to low wavelength resolution near the edge.

To conclude, we have demonstrated that the second-order moment of the strain distribution can be obtained experimentally. The theoretically predicted first and second moments are covered by the 95% confidence interval estimated through Bayesian inference. However, we found out that Gaussian nature of the transmission error could only be established with relatively low confidence. Further work in this area should seek to improve our confidence in the choice of likelihood. Furthermore, the posterior distribution shows direct evidence that the semi-empirical Santisteban model is inadequate for uniquely extracting higher order moments in general. Therefore, a model that explicitly accounts for the moments of the strain distribution and for texture effects in the material is needed. Despite the limitations of the current study, our findings pave the way for neutron strain tomography. The task of more accurate Bragg edge modeling, calibration, and uncertainty quantification is an opportunity for future research.

See the supplementary material for derivation of the Santisteban model.

The authors would like to thank Dr. S. Cotter and Dr. J. Hendriks for their input and ideas at various stages in this project.

This work was funded by EPSRC grants "A Reconstruction Toolkit for Multichannel CT" (No. EP/P02226X/1) and "Rich Nonlinear Tomography for advanced materials" (No. EP/V007742/1). We gratefully acknowledge beamtime No. RB1920056 (https://doi.org/10.5286/ISIS.E.RB1920056)[17] at the IMAT Beamline of the ISIS Neutron and Muon Source, Harwell, UK. K.F. acknowledges the support of the EPSRC grant "EPSRC Centre for Doctoral Training in Agri-Food Robotics" (No. EP/S023917/1) in the final stages of this work. E.A. was partially funded by the Federal Ministry of Education and Research (BMBF) and the Baden-Württemberg Ministry of Science as part of the Excellence Strategy of the German Federal and State Governments. W.R.B.L. acknowledges support from a Royal Society Wolfson Research Merit Award.

AUTHOR DECLARATIONS

Conflict of Interest

The authors have no conflicts to disclose.

DATA AVAILABILITY

The data that support the findings of this study are openly available in embargo at https://doi.org/10.5286/ISIS.E.RB1920056, Ref. 17.

REFERENCES

[1]P. J. Withers and H. Bhadeshia, "Residual stress. Part 1—Measurement techniques," Mater. Sci. Technol. **17**, 355–365 (2001).
[2]M. E. Fitzpatrick and A. Lodini, *Analysis of Residual Stress by Diffraction Using Neutron and Synchrotron Radiation* (CRC Press, 2003).
[3]B. Abbey, S. Y. Zhang, M. Xie, X. Song, and A. M. Korsunsky, "Neutron strain tomography using Bragg-edge transmission," Int. J. Mater. Res. **103**, 234–241 (2012).
[4]S. Vogel, "A Rietveld-approach for the analysis of neutron time-of-flight transmission data," Ph.D. thesis (Christian-Albrechts-University, Kiel, 2000), https://macau.uni-kiel.de/receive/diss_mods_00000330?lang=en.
[5]A. Steuwer, P. Withers, J. Santisteban, L. Edwards, M. Fitzpatrick, M. Daymond, and M. Johnson, "The $\sin^2\psi$-method in pulsed neutron transmission," J. Neutron Res. **9**, 289–294 (2001).
[6]A. S. Tremsin, J. V. Vallerga, J. B. McPhate, O. H. Siegmund, and R. Raffanti, "High resolution photon counting with MCP-Timepix quad parallel readout operating at >1 KHz frame rates," IEEE Trans. Nucl. Sci. **60**, 578–585 (2013).
[7]A. Losko, Y. Han, B. Schillinger, A. Tartaglione, M. Morgano, M. Strobl, J. Long, A. Tremsin, and M. Schulz, "New perspectives for neutron imaging through advanced event-mode data acquisition," Sci. Rep. **11**, 21360 (2021).
[8]W. R. Lionheart and P. J. Withers, "Diffraction tomography of strain," Inverse Probl. **31**, 045005 (2015).
[9]B. Abbey, S. Y. Zhang, W. J. Vorster, and A. M. Korsunsky, "Feasibility study of neutron strain tomography," Procedia Eng. **1**, 185–188 (2009).
[10]B. Abbey, S. Y. Zhang, W. Vorster, and A. M. Korsunsky, "Reconstruction of axisymmetric strain distributions via neutron strain tomography," Nucl. Instrum. Methods Phys. Res., Sect. B **270**, 28–35 (2012).

[11]A. Gregg, J. Hendriks, C. Wensrich *et al.*, "Bragg-edge neutron strain tomography: A review and path forward to general tomographic reconstruction," in *9th Australasian Congress on Applied Mechanics (ACAM9)* (Engineers Australia Sydney, 2017), pp. 274–282.
[12]W. R. Lionheart, "Histogram tomography," Math. Eng. **2**, 55–74 (2020).
[13]G. A. Webster and R. W. Wimpory, "Polycrystalline materials—Determinations of residual stresses by neutron diffraction," ISO/TTA 3:2021 (International Organization for Standardization, Geneva, Switzerland, 2001).
[14]M. Daymond, M. Johnson, and D. Sivia, "Analysis of neutron diffraction strain measurement data from a round robin sample," J. Strain Anal. Eng. Des. **37**, 73–85 (2002).
[15]M. Boin, "Developments towards the tomographic imaging of local crystallographic structures," Ph.D. thesis (The Open University, Milton Keynes, 2011).
[16]G. A. Webster, *Neutron Diffraction Measurements of Residual Stress in a Shrink-Fit Ring and Plug* (National Physical Laboratory, 2000).
[17]W. R. B. Lionheart, G. Burca, A. Korsunsky, M. Turner, J. S. Jørgensen, S. Schmidt, J. Kelleher, K. Yan, P. J. Withers, and E. Ametova, "Can the second moment of the Bragg edge be resolved for neutron strain measurement?," in STFC ISIS Neutron and MuonSource (2019).
[18]G. Burca, W. Kockelmann, J. James, and M. E. Fitzpatrick, "Modelling of an imaging beamline at the ISIS pulsed neutron source," J. Instrum. **8**, P10001 (2013).
[19]W. Kockelmann, T. Minniti, D. E. Pooley, G. Burca, R. Ramadhan, F. A. Akeroyd, G. D. Howells, C. Moreton-Smith, D. P. Keymer, J. Kelleher *et al.*, "Time-of-flight neutron imaging on IMAT@ ISIS: A new user facility for materials science," J. Imaging **4**, 47 (2018).
[20]A. Tremsin, J. McPhate, W. Kockelmann, J. Vallerga, O. Siegmund, and W. Feller, "High resolution Bragg edge transmission spectroscopy at pulsed neutron sources: Proof of principle experiments with a neutron counting MCP detector," Nucl. Instrum. Methods Phys. Res., Sect. A **633**, S235–S238 (2011).
[21]A. Tremsin, J. Vallerga, J. McPhate, and O. Siegmund, "Optimization of Timepix count rate capabilities for the applications with a periodic input signal," J. Instrum. **9**, C05026 (2014).
[22]A. Liptak, G. Burca, J. Kelleher, E. Ovtchinnikov, J. Maresca, and A. Horner, "Developments towards Bragg edge imaging on the IMAT beamline at the ISIS pulsed neutron and muon source: BEAn software," J. Phys. Commun. **3**, 113002 (2019).
[23]J. Santisteban, L. Edwards, A. Steuwer, and P. Withers, "Time-of-flight neutron transmission diffraction," J. Appl. Crystallogr. **34**, 289–297 (2001).
[24]P. Suortti, M. Ahtee, and L. Unonius, "Voigt function fit of x-ray and neutron powder diffraction profiles," J. Appl. Crystallogr. **12**, 365–369 (1979).
[25]F. Kropff, J. Granada, and R. Mayer, "The Bragg lineshapes in time-of-flight neutron powder spectroscopy," Nucl. Instrum. Methods Phys. Res. **198**, 515–521 (1982).
[26]J. R. Santisteban, L. Edwards, M. E. Fitzpatrick, A. Steuwer, P. J. Withers, M. R. Daymond, M. W. Johnson, N. Rhodes, and E. M. Schooneveld, "Strain imaging by Bragg edge neutron transmission," Nucl. Instrum. Methods Phys. Res., Sect. A **481**, 765–768 (2002).
[27]R. Woracek, D. Penumadu, N. Kardjilov, A. Hilger, M. Strobl, R. Wimpory, I. Manke, and J. Banhart, "Neutron Bragg-edge-imaging for strain mapping under *in situ* tensile loading," J. Appl. Phys. **109**, 093506 (2011).
[28]A. Tremsin, J. McPhate, A. Steuwer, W. Kockelmann, A. M. Paradowska, J. Kelleher, J. Vallerga, O. Siegmund, and W. Feller, "High-resolution strain mapping through time-of-flight neutron transmission diffraction with a microchannel plate neutron counting detector," Strain **48**, 296–305 (2012).
[29]A. S. Tremsin, J. B. McPhate, J. V. Vallerga, O. H. Siegmund, W. Kockelmann, A. Paradowska, S. Y. Zhang, J. Kelleher, A. Steuwer, and W. B. Feller, "High-resolution strain mapping through time-of-flight neutron transmission diffraction," in *Materials Science Forum* (Trans Tech Publications, 2014), Vol. 772, pp. 9–13.
[30]J. Hendriks, N. O'Dell, A. Wills, A. Tremsin, C. Wensrich, and T. Shinohara, "Bayesian non-parametric Bragg-edge fitting for neutron transmission strain imaging," J. Strain Anal. Eng. Des. **56**, 371 (2021).
[31]R. S. Ramadhan, W. Kockelmann, T. Minniti, B. Chen, D. Parfitt, M. E. Fitzpatrick, and A. S. Tremsin, "Characterization and application of Bragg-edge transmission imaging for strain measurement and crystallographic analysis on the IMAT beamline," J. Appl. Crystallogr. **52**, 351–368 (2019).
[32]E. T. Jaynes, *Probability Theory: The Logic of Science* (Cambridge University Press, 2003).
[33]M. Betancourt, "A conceptual introduction to Hamiltonian Monte carlo," arXiv:1701.02434 (2017).
[34]R. B. d'Agostino, "An omnibus test of normality for moderate and large size samples," Biometrika **58**, 341–348 (1971).
[35]M. Boin, A. Hilger, N. Kardjilov, S. Zhang, E. Oliver, J. James, C. Randau, and R. Wimpory, "Validation of Bragg edge experiments by Monte Carlo simulations for quantitative texture analysis," J. Appl. Crystallogr. **44**, 1040–1046 (2011).